



# Hypercrosslinked organic polymer based carbonaceous catalytic materials: Sulfonic acid functionality and nano-confinement effect

Jing Li, Xiaochen Wang, Guojian Chen, Difan Li, Yu Zhou\*, Xiaoning Yang, Jun Wang\*

State Key Laboratory of Materials-Oriented Chemical Engineering, College of Chemistry and Chemical Engineering, Nanjing Tech University (former Nanjing University of Technology), Nanjing 210009, China

## ARTICLE INFO

### Article history:

Received 8 February 2015

Received in revised form 4 April 2015

Accepted 28 April 2015

Available online 29 April 2015

### Keywords:

Porous hypercrosslinked polymers

Nano-confinement effect

Catalytic materials

Solid acid catalyst

Carbocatalyst

## ABSTRACT

Porous hypercrosslinked polymers (HCPs) based novel metal-free heterogeneous solid acid catalysts were synthesized via Friedel–Crafts alkylation by self-condensation of bischloromethyl monomers such as  $\alpha,\alpha'$ -dichloro-*p*-xylene and 4,4'-bis(chloromethyl)-1,1'-biphenyl, followed by post-sulfonation process to generate acidic sites. The obtained HCP-based solid acids possessed large amounts of acidic sites homogeneous dispersed over the large surface area of more than  $1000 \text{ m}^2 \text{ g}^{-1}$ , and narrow dispersed pores mostly centered at about 2 nm, the junction region of micro and mesopores. Assessed in Friedel–Crafts alkylation and Beckmann rearrangement reactions, the obtained HCP-based porous solid acid catalysts demonstrated superior performance and special nano-confinement effect in the reactions. These were due to their acidic property and unique pore structure, thus providing an efficient metal-free carbonaceous catalyst for eco-friendly “carbocatalysis” process and some clues to prepare multi-functional catalysts from HCP-based materials.

© 2015 Elsevier B.V. All rights reserved.

## 1. Introduction

“Carbocatalysis” is the process involving the utilization of metal-free carbonaceous materials (mainly bearing typical organic elements like C, H, N, O, etc.) as catalysts for heterogeneous catalysis [1–4] and has gained increasing attentions due to the requirement of sustainable development facing with environmental pollution and energy shortness. Heterogeneous metal-free catalysts combine advantages of traditional heterogeneous catalysis (e.g., facile separation and recycling of catalysts) and avoidance of employing metals that leach in catalytic processes, which therefore possess the characteristic of ecologically viable, highly stable, noncorrosive and sustainable [5,6]. However, only limited metal-free heterogeneous catalysts presented comparable performance as the metal-containing ones [7,8], thus it is of great challenge to develop new efficient metal-free carbonaceous catalyst towards environmental friendly process, meeting the criteria to fabricate and disperse high-quality active sites on the large surface framework [5,9,10]. One efficient way is to control the pore structure that has been found to be crucial for catalytic performance [11–13].

Many approaches have been proposed to develop metal-free catalysts [3,14,15], among which, functionalized porous organic polymers (POPs) are widely studied due to the high chemical and thermal stability, highly accessible internal surface usually with hydrophobicity, controllable pore structure, and a wide range of chemical functionalities [16–19]. The metal-free POP-based catalysts have been applied in acid, basic and oxidation reactions [12,20–22]. It is known that the structure of nanometer sized cavities in porous catalyst may enhance catalytic activity [13,23], and POPs can afford nanospace environments, capable of binding and transforming small molecule substrates [16]. Nevertheless, rare studies have focused on the influence of the pore structure, especially the nanometer sized cavities, on the catalytic activity [24], because most POP-based metal-free catalysts usually own relatively wide and irregular pore size dispersion [25,26].

As one kind of POPs, porous hypercrosslinked polymers (HCPs) possess high surface areas, hydrophobicity-derived superior organic compatibility, and well chemical and thermal stability [27,28]. HCPs are produced from bulk chemicals via Friedel–Crafts alkylation catalyzed by anhydrous  $\text{FeCl}_3$ , which avoids the use of noble metal coupling catalysts and the strict requirement of monomers with specific polymerisable groups [29], therefore it is a facile and low cost way to fabricate functional POPs materials. So far, many studies have focused on the application of HCPs as the supports of metals for heterogeneous catalysis [30]. For example, Li et al. [31] prepared Pd(II) organometallic catalysts immobilized

\* Corresponding authors. Tel.: +86 25 83172264; fax: +86 25 83172261.

E-mail addresses: [njutzhouyu@njtech.edu.cn](mailto:njutzhouyu@njtech.edu.cn) (Y. Zhou), [junwang@njtech.edu.cn](mailto:junwang@njtech.edu.cn) (J. Wang).

on the triphenylphosphine-functionalized KAPs(Ph-PPh<sub>3</sub>), where the porous structure of support ensured the high dispersion of Pd active sites and easy diffusion of organic reactant molecules in the pore channel. Besides, HCPs have also shown attractive potential for heterogeneous organocatalysts, though only few reports appeared. For instance, Bhaumik and co-workers [3] constructed highly crosslinked carboxyl-bearing organic polymer (COP-A) and applied it as a heterogeneous carbocatalyst for indole C–H substitution reactions, which is unique among the class of carbocatalysts due to the high concentration of active sites attached covalently to the high-surface-area polymer skeleton.

Sulfonation is a widely adopted effective strategy to prepare novel solid acid catalysts, but it has never been subjected to HCPs materials. In this work, sulfonic acid (–SO<sub>3</sub>H)-functionalized HCPs materials with high surface areas are developed and applied as solid acid catalysts, which are fabricated from self-condensation of the rigid bischloromethyl monomers ( $\alpha,\alpha'$ -dichloro-*p*-xylene or 4,4'-bis(chloromethyl)-1,1'-biphenyl) through FeCl<sub>3</sub>-induced Friedel–Crafts alkylation, followed with introducing –SO<sub>3</sub>H groups by the post-sulfonation (Scheme 1). The pore structure is simultaneously adjusted by controlling the sulfonation process. Catalytic performances of these functionalized HCPs are evaluated in the two acid-catalyzed reactions: Friedel–Crafts alkylation and Beckmann rearrangement. Influences of amount of acid sites and feature of pore structure on catalytic activities are systematically studied, with comparisons with various control solid acid catalysts.

## 2. Experimental

### 2.1. Materials

All chemicals and solvents were commercially available and used as received unless otherwise stated.  $\alpha,\alpha'$ -dichloro-*p*-xylene (DCX) and 4,4'-bis(chloromethyl)-1,1'-biphenyl (BCMP) were purchased from Aladdin Reagent Corp. Anhydrous ferric trichloride (FeCl<sub>3</sub>), anhydrous dichloroethane (DCE), anhydrous dichloromethane (DCM) and chlorosulfonic acid (ClSO<sub>3</sub>H) were analytical grade and purchased from Shanghai Lingfeng Chemical Reagent Co., Ltd.

### 2.2. Catalyst preparation

Functionalized hypercrosslinked organic polymers were prepared by self-condensation of bischloromethyl monomers (DCX or BCMP). Anhydrous FeCl<sub>3</sub> (40 mmol) was dissolved in anhydrous DCE (20 mL) and then added into the solution containing 20 mmol monomer and 20 mL DCE under nitrogen atmosphere. The resulting mixture was heated using standard thermal heating and stirred at 80 °C for 24 h. The obtained brown precipitate was separated by filtration, washed three times with methanol, followed with extraction in a Soxhlet extractor with methanol for 24 h and ultimately dried at 100 °C for 12 h (99% yield) [32]. Sulfonation of hypercrosslinked organic polymers was performed by treating with chlorosulfonic acid in anhydrous DCM. Typically, 1.0 g of the polymer sample was outgassed at 100 °C in a three-necked round flask for 3 h. Then, 20 mL of DCM containing chlorosulfonic acid (4 mL) was slowly added into the flask at 0 °C and the mixture was stirred for 12 h under nitrogen atmosphere. Finally, the acid-functionalized product was obtained by filtration, washing with anhydrous DCM, extraction in a Soxhlet extractor with methanol for 24 h, and drying at 100 °C for 12 h. The C, H, S elemental analysis data for all the hypercrosslinked polymers were listed in Table S1. The deviations between theoretical and experimental values were observed on these polymers due to the incomplete alkylation and trapped adsorbates including catalyst, gases and water

vapor within the pores, which are consistent with previous reports [33–35].

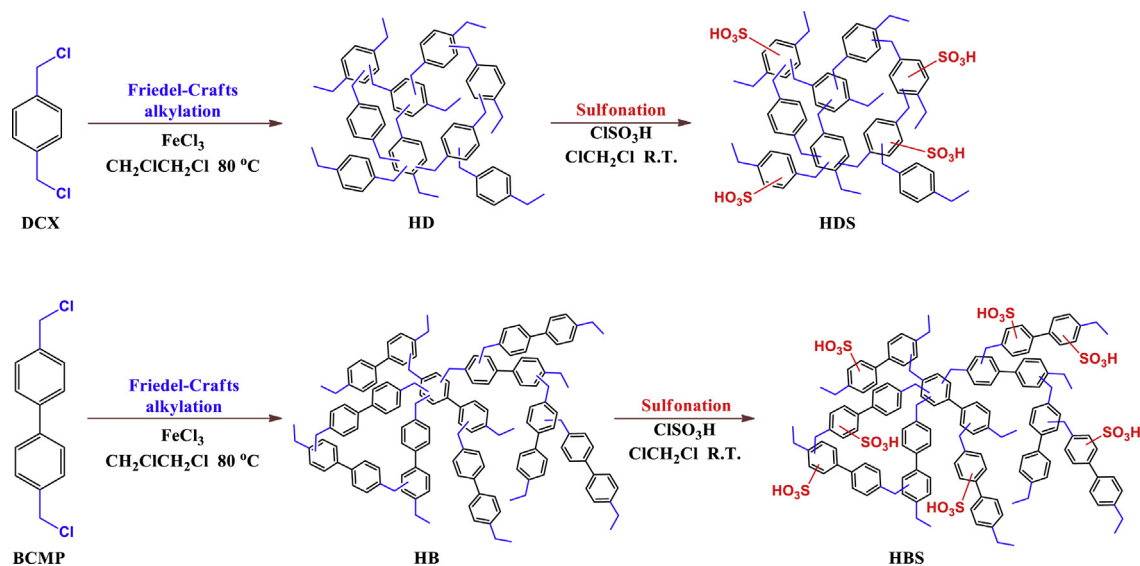
For comparison, mesoporous polydivinylbenzene (PDVB) was synthesized according to the literature [36]. PDVB was hydrothermally synthesized by polymerization with the starting system of DVB/2,2-azobisisobutyronitrile/tetrahydrofuran/water at molar ratio of 1/0.02/16/7.23. The mixture was hydrothermally treated at 100 °C for 48 h. Sulfonation of PDVB was performed by treating with chlorosulfonic acid in anhydrous DCM, and the obtained sample was denoted as PDVBS. The other two commonly seen solid acids, SBA-15-S (sulfonic acid-modified mesoporous silica SBA-15) and H-beta (hydrogen form of zeolite beta), were prepared according to the previous literatures (details are in Supporting information) [37,38].

### 2.3. Characterization

Fourier transform infrared (FT-IR) spectra were recorded on a Nicolet iS10 FT-IR instrument (KBr disks) in the 4000–400 cm<sup>–1</sup> region. Raman Spectra were obtained using a Horiba HR 800 spectrometer. As a source of excitation, the 514 nm line of a Spectra Physics 2018 Argon/Krypton Ion Laser system were focused through an Olympus BX41 microscope equipped with a 50 magnification objective. Nitrogen (N<sub>2</sub>) adsorption isotherms and Brunauer–Emmett–Teller (BET) surface areas were measured at the temperature of liquid nitrogen (–196 °C) by using a BELSORP-MINI analyzer, and the samples were degassed at 150 °C for 3 h to a vacuum of 10<sup>–3</sup> Torr before analysis. The C, H, S elemental analysis was performed on an elemental analyzer Vario EL cube. Nuclear magnetic resonance (NMR) experiments were carried out on a Bruker Avance III spectrometer in a magnetic field strength of 11.7 T. The <sup>13</sup>C cross-polarization (CP)/magic-angle-spinning (MAS) NMR were performed with a contact time of 2.0 ms, a recycle delay of 15.0 s, and a sample spinning rate of 6 kHz. Thermo gravimetry (TG) analysis was carried out with a STA409 instrument in dry air at a heating rate of 10 °C min<sup>–1</sup>. Field emission scanning electron microscope (FESEM; Hitachi S-4800, accelerated voltage: 5 kV) accompanied by Energy dispersive X-ray spectrometry (EDS; accelerated voltage: 20 kV) was used to study the morphology and the elements distribution. Transmission electron microscope (TEM) images were obtained by using a JEOL JEM-2010 (200 kV) TEM instrument. The acid-exchange capacity was determined by dispersing catalysts in aqueous solution of NaCl through a typical acid-base titration with NaOH solution. The surface chemical composition of the samples was determined by X-ray photoelectron spectroscopy (XPS) on a PHI 5000 Versa Probe X-ray photoelectron spectrometer equipped with Al K $\alpha$  radiation (1486.6 eV). X-ray diffraction (XRD), NH<sub>3</sub>-temperature programmed desorption (NH<sub>3</sub>-TPD) and solid ultraviolet-visible (UV–vis) adsorption spectra are described in Supporting information.

### 2.4. Catalytic tests

Friedel–Crafts alkylation reaction of anisole and benzyl alcohol was carried out in a 25 mL round-bottom flask equipped with a reflux condenser and a magnetic stirrer. In a typical run, anisole (20 mmol), benzyl alcohol (4 mmol), and catalyst (0.1 g) were taken into the flask. The resultant mixture was heated at 120 °C for 4 h. After reaction, the internal standard *n*-hexadecane was added and analyzed by a gas chromatography (GC, Shimadzu GC-2014) equipped with a flame ionization detector and a capillary column (SE-30, 50 m  $\times$  0.25 mm  $\times$  0.6  $\mu$ m). Besides the major alkylation product methoxydiphenylmethane (MDM) (including *p*-MDM and *o*-MDM), only dibenzyl ether (DBE) was detected as the by-product under the employed conditions.



**Scheme 1.** Synthesis of sulfonic acid functionalized hypercrosslinked bischloromethyl-based porous organic polymers (DCX:  $\alpha,\alpha'$ -dichloro-*p*-xylene, BCMP: 4,4'-bis(chloromethyl)-1,1'-biphenyl).

Beckmann rearrangement of cyclohexanone oxime was carried out in a 25 mL round-bottomed flask. Typically, the solvent of benzonitrile (PhCN) (4 mL), cyclohexanone oxime (1 mmol) and catalyst (0.1 g) were charged into the flask reactor successively to make a reaction mixture, which was then heated at 130 °C for 6 h. At the end of the reaction the resulting product mixture was cooled down and the internal standard *n*-dodecane was added. Quantitative analyses were conducted with gas chromatography (GC, Agilent GC 7890B) equipped with a flame ionization detector and a capillary column (HP-5, 30 m  $\times$  0.25 mm  $\times$  0.25  $\mu$ m). The major rearrangement product was  $\epsilon$ -caprolactam (CPL), and the detected by-product was cyclohexanone generated from the side-reaction of the hydrolysis of cyclohexanone oxime. Other possible by-products like cyclohexen-1-one, nitriles and dimers were in trace amount.

### 3. Results and discussion

#### 3.1. Synthesis and pore structure of -SO<sub>3</sub>H functionalized HCPs

Scheme 1 illustrates the two steps for preparing the functionalized HCP-based solid acid materials: 1) bischloromethyl monomers are self-cross-linked through a Friedel–Crafts alkylation process to give the HCP products that are insoluble in common organic solvents and water; 2) the acidic sites, -SO<sub>3</sub>H groups, are introduced through a post-sulfonation route by treating the HCP materials obtained in the first step with ClSO<sub>3</sub>H. Two monomers (DCX and BCMP) are selected in the synthesis and the obtained HCP materials are named as HD and HB, respectively. The finally resultant solid acid materials are denoted as HDS-*x* and HBS-*x* (*x* = 1, 2, 4, 8 and 16), in which *x* is index of the ClSO<sub>3</sub>H amounts (mL per gram of HCPs) used in the sulfonation step.

Theoretically, each chloromethyl group should be converted into a methylene bridge by elimination of one hydrogen chloride molecule in the alkylation reaction. But in fact, the residual chlorine in the resulting polymer is found according to EDS (Fig. S1), indicating that there are chloromethyl groups that remain unsubstituted in the first step. Similar results are also reported by other groups with residual chlorine or bromine in the HCPs [33].

Fig. 1A and C display the N<sub>2</sub> sorption results of all the two series of HCP materials, with the related textural properties being summarized in Table 1. Both N<sub>2</sub> sorption isotherms of HD and HB follow a steep nitrogen uptake at low  $P/P_0$  ( $P/P_0 < 0.001$ ), typically for

microporosity, and the further steady increase in adsorption occurs at high pressure region ( $P/P_0 = 0.5$ – $0.9$ ) on account of the wide scale mesoporosity. The hysteresis of HD in the high pressure region ( $P/P_0 > 0.9$ ) implies the existence of interparticle mesopores voids or cages. The nonlocal density functional theory (NLDFT) pore size distribution curves (Fig. 1B and D) are calculated using the cylinder-pore model. The sample HD shows a bimodal porosity with the most probable pore diameters at ca. 0.85 and 2.2 nm, while HB similarly presents a sharp peak at 0.85 nm and a wider one at 2.2 nm, but adding a narrow peak at 2.5 nm and a very wide one centered at ca. 6 nm. The parent materials of HD and HB possess high surface areas of 1335 and 1900 m<sup>2</sup> g<sup>-1</sup>, respectively.

The N<sub>2</sub> sorption isotherms of HDS-*x* and HBS-*x* are similar to the parent samples HD and HB, exhibiting similar uptakes index of micropores and mesopores, but these -SO<sub>3</sub>H modified samples possess relatively lower surface areas than their parents. Along with increasing of chlorosulfonic acid amounts (*x*) used in sulfonation treatment, the surface areas of HDS-*x* and HBS-*x* series continuously decrease until *x* = 8, while the pore volume first decreases, and then increases when *x* is beyond 4, with the minimum value observed at *x* = 4. As for the average pore diameter, it first declines and then rises, achieving the minimum at *x* = 4. The pore size distribution curve also indicates that the micropore is decreasing during the sulfonation process while the pores centered at ca. 2 nm are preserved. The enlargement of the average pore diameter at high *x* conditions can be attributed to the emerging of macropores as observed in the pore size distribution curves, which is more apparent for HDS-*x* than HBS-*x*. During the sulfonation process for HD and HB, the polymeric framework reacts with chlorosulfonic acid with the formation of the attached -SO<sub>3</sub>H groups on framework, but also accompanied with the collapse and rearrangement of the pore structure. Two factors affect above pore variation. One is the filling of -SO<sub>3</sub>H groups in the pores that narrows the initially existing pores, in other words, the pore blockage contributes to the gradual disappearance of small pores. Another is the corrosion of the polymeric skeleton, especially in the presence of excessive chlorosulfonic acid, causing the decrease of mesopores [39]. An obvious evidence for the corrosion process is the formation of a large amount of macropores. Therefore, increasing the degree of sulfonation gradually causes the disappearance of small pores, the decrease of mesopores, and the formation and increase of macropores. The surface area first decreases due to partial pore blockage,

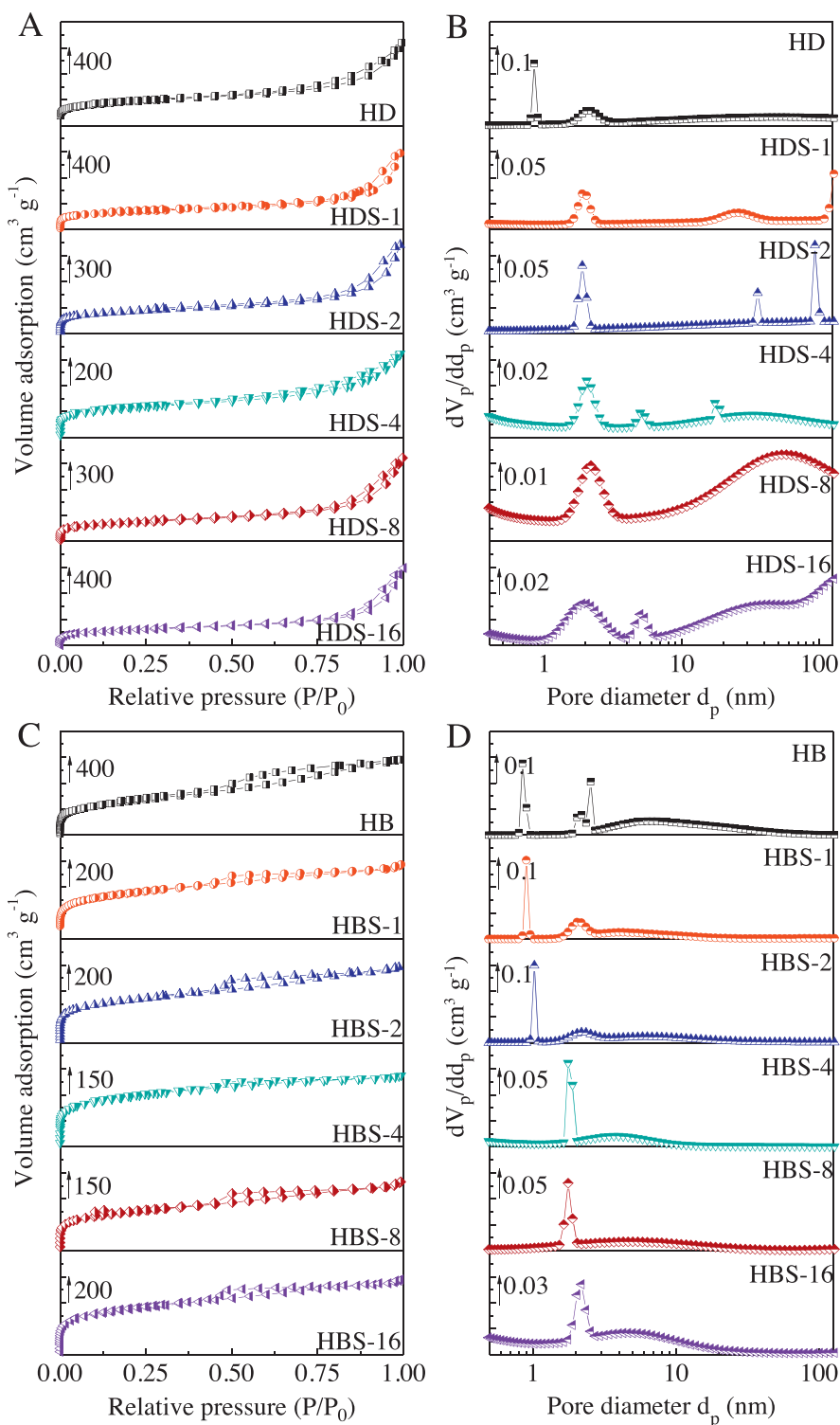


**Fig. 1.** (A and C)  $N_2$  sorption isotherms and (B and D) pore size distribution curves of various HCP materials.

and then increases in the sample HDS-16 and HBS-16 due to the formation of additional pores.

### 3.2. Further structural characterizations

The typical  $-SO_3H$  functionalized HCP materials HDS-4 and HBS-4, as well as their parent counterparts HD and HB, are selected to be further characterized by FT-IR, NMR, Raman, TG, XPS, FESEM,

TEM, XRD and UV-vis analyses. In FT-IR spectra (Fig. 2A), all the four samples display the band at about  $2920\text{ cm}^{-1}$  ascribed to C–H stretching vibrations for  $-CH_2-$  in DCX or BCMP monomer [35], suggesting that the basic structures of monomers are preserved during cross-linking and sulfonation processes. For HDS-4 and HBS-4, the bands at around  $670$  and  $1280\text{ cm}^{-1}$  for stretching and wagging vibrations from the  $-CH_2-Cl$  group of DCX or BCMP [35] remain very weak, implying a successful self-condensation of

**Table 1**

Textural and acidic parameters of various solid acid catalysts.

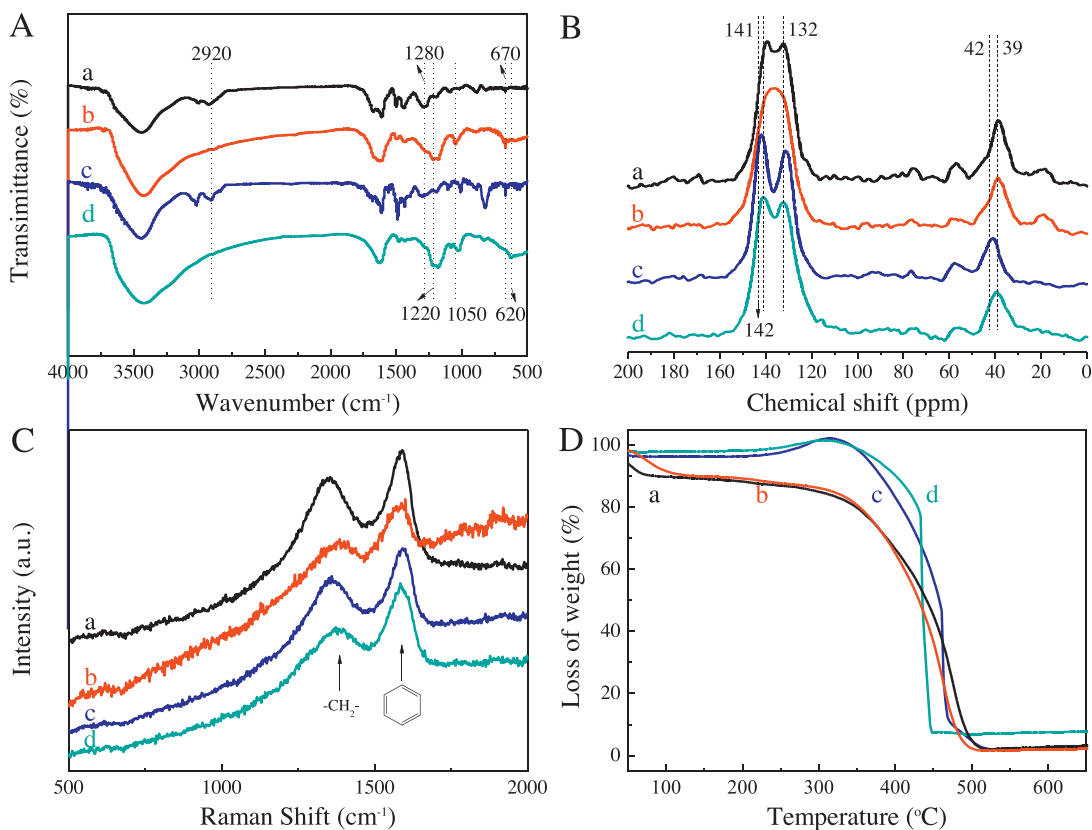
Run	Samples	S content (mmol g <sup>-1</sup> ) <sup>a</sup>	Acid amount (mmol g <sup>-1</sup> ) <sup>b</sup>	S <sub>BET</sub> (m <sup>2</sup> g <sup>-1</sup> ) <sup>c</sup>	V <sub>P</sub> (cm <sup>3</sup> g <sup>-1</sup> ) <sup>d</sup>	D <sub>P</sub> (nm) <sup>e</sup>	D <sub>ave</sub> (nm) <sup>f</sup>
1	HD	0	0	1335	1.87	0.85	5.61
2	HDS-1	0.59	0.65	996	1.79	1.89	7.18
3	HDS-2	0.73	0.79	927	1.57	1.89	6.77
4	HDS-4	0.82	0.83	825	0.99	2.04	4.79
5	HDS-8	0.81	0.82	790	1.41	2.19	7.16
6	HDS-16	0.82	0.84	850	1.71	1.89	8.05
7	HB	0	0	1900	1.80	0.85	3.79
8	HBS-1	1.90	1.92	1280	1.04	0.90	3.25
9	HBS-2	1.99	2.02	1189	0.90	1.02	3.03
10	HBS-4	2.06	2.29	1037	0.63	1.76	2.45
11	HBS-8	2.14	2.30	887	0.69	1.76	3.11
12	HBS-16	2.28	2.41	1080	0.89	2.19	3.30
13	H-beta	–	1.21	574	0.49	–	3.43
14	SBA-15-S	1.37	1.28	544	1.71	–	12.6
15	H <sub>2</sub> SO <sub>4</sub>	10.2	20.4	–	–	–	–
16	Amberlyst-15	4.30	4.70	45	0.31	–	40.0

<sup>a</sup> Measured by elemental analysis.<sup>b</sup> Measured by acid–base titration.<sup>c</sup> BET surface area.<sup>d</sup> Total pore volume.<sup>e</sup> The most probable pore size of HCP-based materials are calculated according to the NLDFT.<sup>f</sup> Average pore size estimated from BJH model.

the monomers. Also compared with HD and HB, HDS-4 and HBS-4 exhibit an additional peak around 1050 cm<sup>-1</sup> associated with the stretching vibration of C–S bond, and the other two bands at ca. 620 and 1220 cm<sup>-1</sup> assigned to symmetric and asymmetric stretching signals of O=S=O bonds in sulfonic groups [40]. The above observation indicates the successful introduction of sulfonic groups onto the framework of porous hypercrosslinked polymers.

In the <sup>1</sup>H-<sup>13</sup>C CP/MAS NMR spectra (Fig. 2B), three main peaks are observed for all the four materials at ca. 39, 132, and 141 ppm,

which are assigned to methylenes (39 ppm), non-substituted (*i.e.*, hydrogen-bearing) aromatic carbons (132 ppm), and substituted aromatic carbons (141 ppm), respectively [34,35]. There is a signal at ca. 39 ppm, implying a highly hyper-cross-linking degree. The minor resonance at ca. 42 ppm is attributable to the <sup>13</sup>C-<sup>35,37</sup>Cl residual dipolar coupling from the unconsumed –CH<sub>2</sub>–Cl groups [32]. A peak at around 142 ppm resulted from the aromatic carbon coordinated with –SO<sub>3</sub>H group is observed on HDS-4 and HBS-4, further confirming the successful sulfonation on the aromatic rings

**Fig. 2.** (A) FT-IR spectra, (B) <sup>1</sup>H-<sup>13</sup>C CP/MAS NMR spectra, (C) Raman spectra and (D) TG curves of (a) HD, (b) HDS-4, (c) HB and (d) HBS-4.



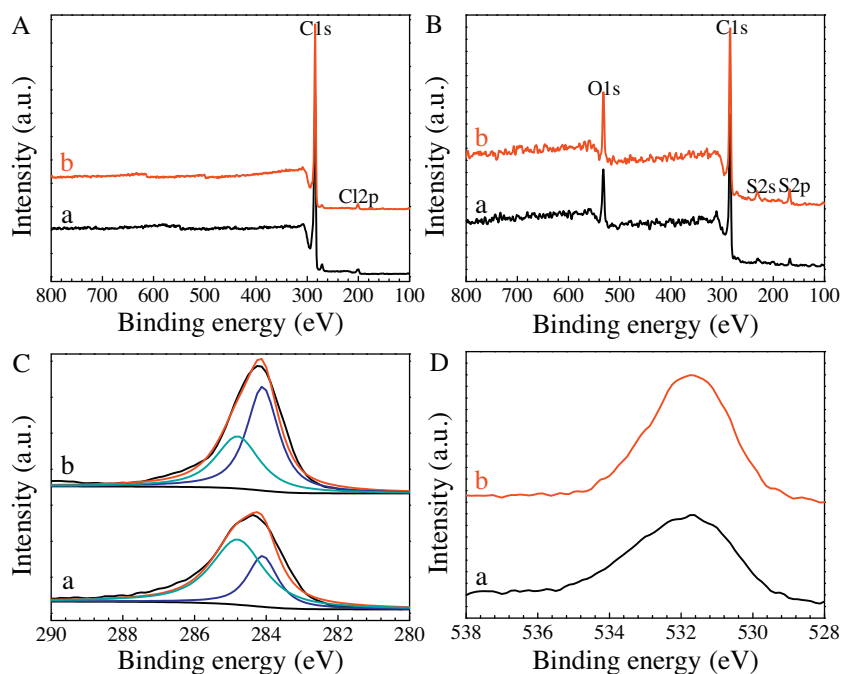


Fig. 3. X-ray photoelectron spectroscopy measurements of (A) survey of (a) HD and (b) HB, (B) survey, (C) C1s, (D) O1s of (a) HDS-4 and (b) HBS-4.

in HD and HB [41]. The two remarkable peaks at 132 and 141 ppm become adjacent in the spectra of HDS-4 and HBS-4, and change to be almost one peak in the spectrum of HDS-4. The above variation of NMR signals in the range of 130–145 ppm for the samples before and after sulfonation can be assigned to that the non-substituted aromatic carbon is affected by the adjacent one tethered with  $-\text{SO}_3\text{H}$  group [33,41]. The resonance at around 55 ppm is the spinning side band [32].

The HCP-based materials are also identified by Raman spectroscopy (Fig. 2C). The bands originating from the methylene ( $1350\text{ cm}^{-1}$ ) and phenyl ( $1600\text{ cm}^{-1}$ ) groups are clearly ascertained [42,43], testifying that the basic structures of monomers are preserved during the self-condensation and sulfonation processes. Compared with HD/HB, HDS-4/HBS-4 shows a slightly decreased intensity of Raman signals due to the introduction of acidic groups. It is also noteworthy that the position and shape of each peak dose not shift after sulfonation, implying the maintaining of the skeleton structure in the functionalized HCPs materials.

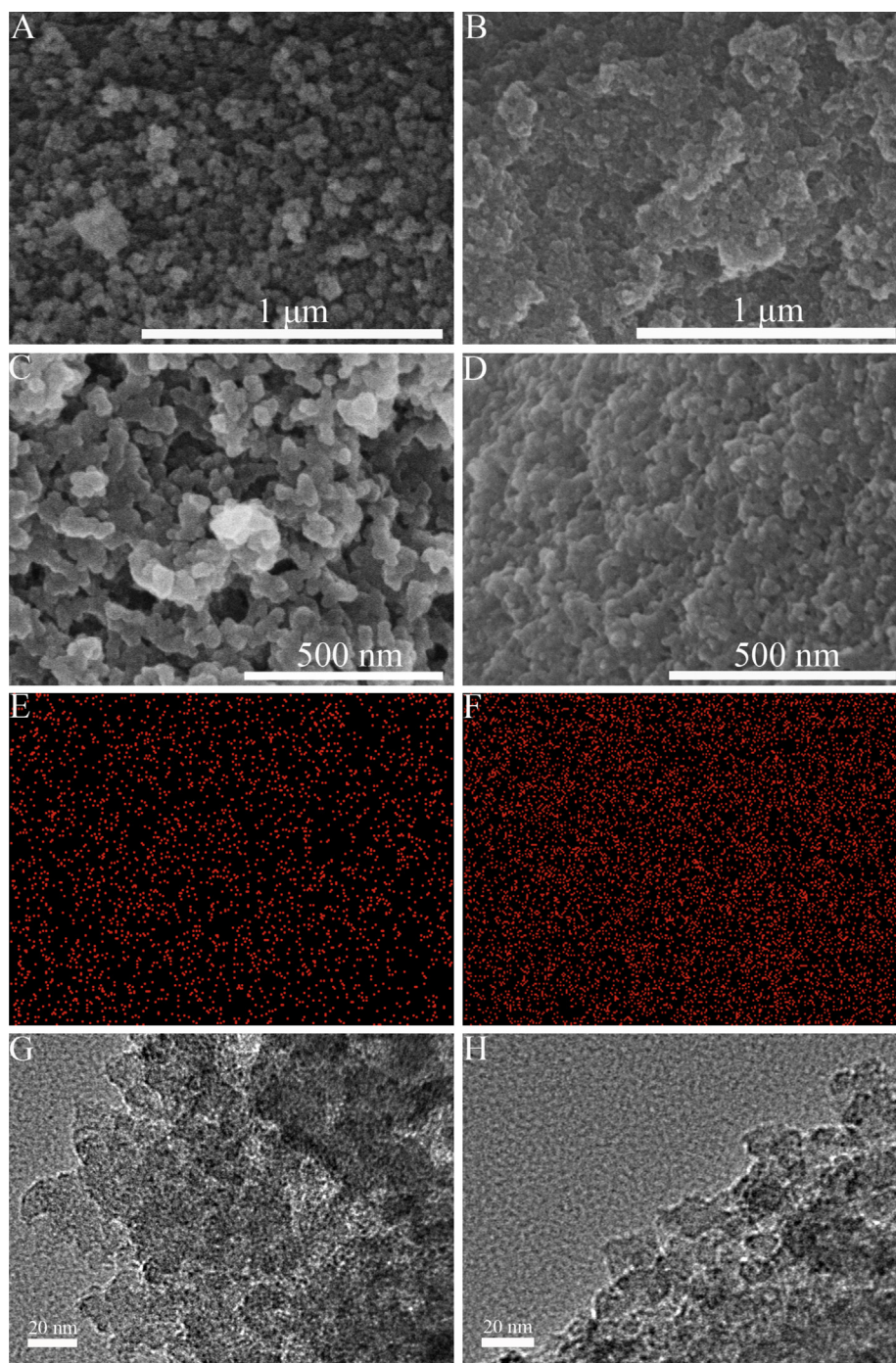
The extensive hypercrosslinked skeleton may facilitate the highly robust character of HCPs, including chemical and thermal stability. TG analysis (Fig. 2D) indicates that these polymers are thermally stable at least up to  $300^\circ\text{C}$  in air, higher than that of the commercial polymeric solid acid Amberlyst-15 ( $250^\circ\text{C}$ ) [44], which demonstrates the superior framework stability of the present HCP-based solid acids derived from their special monomer structure and cross-linking mode. As weaker stability of methylene linkers compared with aromatic rings [35], HD and HDS-4 begin to degrade at approximately  $300^\circ\text{C}$ , while HB and HBS-4 are able to endure the higher temperature of  $350^\circ\text{C}$ , indicating that BCMP-derived HCPs are more stable than the ones derived from DCX. The curves of HB and HBS demonstrate a rise tendency near  $300^\circ\text{C}$ , which might be ascribable to the adsorption of carbon dioxide, water vapor and/or other unknown compounds in air. Such phenomenon also happened previously [35]. The similar curves of  $-\text{SO}_3\text{H}$  functionalized samples to their parents suggest that the sulfonation treatment have not hampered their thermal stability.

Fig. 3 shows the XPS spectra of HD, HB, HDS-4 and HBS-4. Clearly, the samples HD and HB show the signals of C1s (284.2 eV) and Cl2p

(300.0 eV) (Fig. 3A). The weak signal at 300.0 eV is attributable to C–Cl in the monomer, in accordance with the EDS result mentioned above. The functionalized samples show the signals of S2p (168.2 eV), S2s (231.3 eV), C1s (284.2 eV), and O1s (531.7 eV) (Fig. 3B), validating the presence of sulfonic groups [43]. The signal of Cl2p (300.0 eV) can be neglected relative to the ones of S. The high-resolution XPS spectrum for C1s of HDS-4 and HBS-4 is fitted and deconvoluted into two peaks at ca. 284.1 and 284.8 eV (Fig. 3C), which can be assigned to C–C in the major network, and C–S in the sulfonic group [45–47]. The S2p and S2s spectra give only weak signals due to the comparatively low amount of S atoms on the surface of polymer. The high-resolution O1s spectra show a single Gaussian distribution peak at 531.7 eV that is ascribed to the bond energy site of O–S in the sulfonic group (Fig. 3D). The above results confirm the grafting of sulfonic groups onto the HCP networks, in good agreement with FT-IR and elemental analysis results (Fig. 2A, Table S1).

The morphology is investigated by FESEM images. As shown in Fig. 4A–D, all the four HCP materials are consisted of analogous spherical particles, typical for conventional HCP materials. The primary particles of HD and HB are relatively irregular agglomerated nanoparticles with a size of about 40 nm, whereas HDS-4 and HBS-4 are composed by very tiny irregular fused ellipses with diameters of roughly 20 nm. The nano-sized primary particles for all these HCP samples are closely interacted and packed into large aggregates, forming a globular structure. Elemental mapping analyses with EDS for S element (Fig. 4E and F) indicate the successful introduce of  $-\text{SO}_3\text{H}$  groups with homogeneous distribution in the porous network. The TEM images (Fig. 4G and H) show worm-like porous structure for these materials.

Additionally, XRD patterns show only a very broad peak, index of amorphous nature of these HCPs (Fig. S2A), due to disordered linkage among the building units of frameworks. It is typically resulted from the distortion of the phenyl rings and substitution at *para*- and *ortho*-positions [48]. UV–vis adsorption spectra (Fig. S2B) give a broad absorption across the wavelength range 200–600 nm, consistent with other reported networks [49,50].



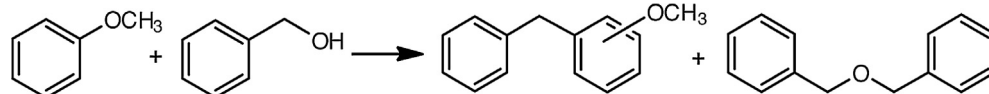
**Fig. 4.** FESEM images of (A) HD, (B) HB, (C) HDS-4 and (D) HBS-4 with EDS mapping (S element) of (E) HDS-4 and (F) HBS-4, and TEM images of (G) HDS-4 and (H) HBS-4.

### 3.3. Acid properties of catalysts

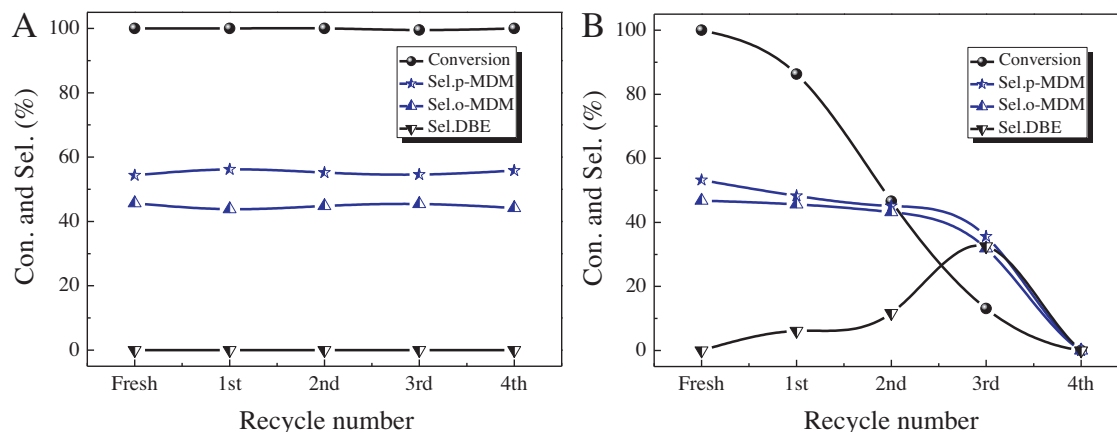
Table 1 lists S content (from elemental analysis) and acid amount (from acid–base titration) for all the  $-\text{SO}_3\text{H}$  functionalized HCP-based materials, as well as the control catalysts. As more and more chlorosulfonic acid is used for sulfonation, both S content and the related acid amount apparently increase in the initial stage, arriving a relative high value at  $x = 4$ , and then keep constant for HDS- $x$  series or go on with slight ascent for HBS- $x$  series. The largest amount of acid sites is found at 0.84 and  $2.41 \text{ mmol g}^{-1}$  over HDS-16 and HBS-16, respectively. Notably, HBS- $x$  (run 8–12) have relatively higher concentration of acid sites ( $1.92 \sim 2.41 \text{ mmol g}^{-1}$ ) than microporous H-beta ( $1.21 \text{ mmol g}^{-1}$ , run 13) and mesoporous SBA-15-S

( $1.28 \text{ mmol g}^{-1}$ , run 14). The above results further verify the introduction of  $-\text{SO}_3\text{H}$  groups into HCPs networks, forming considerably high amounts of  $-\text{SO}_3\text{H}$ -related Brønsted acid sites. It seems that there existed a saturation capacity for polymeric matrix to tether  $-\text{SO}_3\text{H}$  groups, rather than that all the benzene rings can be loaded with  $-\text{SO}_3\text{H}$  groups. The benzene rings are hypercrosslinked to form the polymeric framework and only the benzene rings exposing on the surface of open pores can be sulfonated. Therefore, a saturated amount of acid sites is observed even treated with excessive acid.

The acid properties of HD, HDS, HB and HBS samples are probed by  $\text{NH}_3$ -TPD curves shown in Fig. S3. Straight and horizontal lines are observed over HD and HB samples, indicative of lacking acidic sites, in accordance with the results of elemental analysis. By con-

**Table 2**Catalytic activities of various HCP-based materials and control samples for Friedel–Crafts alkylation.<sup>a</sup>

Run	Catalyst	Con. (%) <sup>b</sup>	Sel. (%)		TON <sup>e</sup>
			MDM ( <i>p</i> -MDM, <i>o</i> -MDM) <sup>c</sup>	DBE <sup>d</sup>	
1	HD	0	–	–	0
2	HDS-1	83.0	51.9 (30.4, 21.5)	48.1	26.5
3	HDS-2	95.3	61.3 (35.4, 25.9)	38.7	29.6
4	HDS-4	99.9	89.0 (50.6, 38.4)	11.0	42.9
5	HDS-8	99.9	79.5 (44.8, 34.7)	20.5	38.4
6	HDS-16	99.9	66.8 (38.0, 28.8)	33.2	29.4
7	HB	0	–	–	0
8	HBS-1	99.9	100 (53.6, 46.4)	0	20.8
9	HBS-2	99.9	100 (54.3, 45.7)	0	19.8
10	HBS-4	99.9	100 (52.9, 47.1)	0	17.5
11	HBS-8	99.9	100 (54.2, 45.8)	0	17.4
12	HBS-16	99.9	100 (53.7, 46.3)	0	16.6
13	H-beta	40.7	57.9 (32.8, 25.1)	42.1	7.8
14	SBA-15-S	48.2	66.1 (36.0, 30.1)	33.9	10.0
15	H <sub>2</sub> SO <sub>4</sub>	99.9	100 (55.1, 44.9)	0.0	2.0
16	Amberlyst-15	99.9	100 (53.2, 46.8)	0.0	8.5

<sup>a</sup> Reaction conditions: benzyl alcohol (4 mmol), anisole (20 mmol), catalyst (0.1 g), 120 °C, 4 h.<sup>b</sup> Con. (%) = (mmol *p*-MDM + mmol *o*-MDM + mmol DBE)/mmol initial benzyl alcohol × 100.<sup>c</sup> Sel. MDM (%) = (mmol *p*-MDM + mmol *o*-MDM)/(mmol *p*-MDM + mmol *o*-MDM + mmol DBE) × 100; the values within parentheses are selectivity of *p*-MDM and *o*-MDM, respectively.<sup>d</sup> Sel. DBE (%) = mmol DBE/(mmol *p*-MDM + mmol *o*-MDM + mmol DBE) × 100.<sup>e</sup> TON: alkylation products (mol) produced on per molar acid site.**Fig. 5.** Catalytic recyclability over (A) HBS-4 and (B) Amberlyst-15 for Friedel–Crafts alkylation reaction of anisole with benzyl alcohol.

trast, HDS-4 and HBS-4 show two main NH<sub>3</sub> desorption peaks at relative high temperatures. Normally, the strength of acid sites are typically distinguished by desorption temperatures of NH<sub>3</sub>: 150–250 °C, 250–350 °C, 350–500 °C and >500 °C are respectively measured as weak, medium, strong and super-strong acid sites [46]. As seen in Fig. S3, medium and strong acid sites obviously exist in HDS-4 and HBS-4. Fitting NH<sub>3</sub>-TPD profiles with multiple peaks, the amounts of acid sites for the medium and strong acid sites can be estimated by calculating the desorption peak area of ammonia and the acid strength is reflected by the maximum peak temperature ( $T_{\max}$ ) of desorption peak [51]. The densities for surface acidic sites are obtained by deconvolution and integration of NH<sub>3</sub>-TPD traces as presented in Table S2. HDS-4 exhibits two peaks (335 °C and 445 °C), corresponding to medium and strong acid sites. By integrating the peak area, it could be found that the total acidity of HDS-4 is 0.91 mmol g<sup>-1</sup> [52], in which the strong and medium acidity are 0.53 and 0.38 mmol g<sup>-1</sup>, respectively. Also, HBS-4 exhibits medium (335 °C, 1.34 mmol g<sup>-1</sup>) and strong acid sites (455 °C, 0.98 mmol g<sup>-1</sup>), with the total acidity of 2.32 mmol

g<sup>-1</sup>. The above results indicate that HD and HB possess no acid sites and plenty of medium and strong acid sites are formed after sulfonation. Accordingly, HBS-4 has over three times more total acid sites than HDS-4, which may lead to the high catalytic activity and durability of HBS-4 [53].

### 3.4. Catalytic activities

Catalytic performances of the obtained HCP-based solid acids are evaluated in Friedel–Crafts reaction and Beckmann rearrangement. Table 2 compares catalytic activities of HCP materials and various control samples in Friedel–Crafts alkylation of anisole with benzyl alcohol, in which MDM are the major products while DBE is the by-product from dehydration of benzyl alcohol. The reaction cannot proceed in the absence of a catalyst [40]. The parent samples HD and HB are not active for this reaction due to the lack of acidic sites (run 1 and 7). HDS-1 exhibits a low conversion of 83.0% (based on benzyl alcohol) and selectivity of 51.9% to MDM (run 2). The conversion increases to 95.3% with slight higher selectiv-



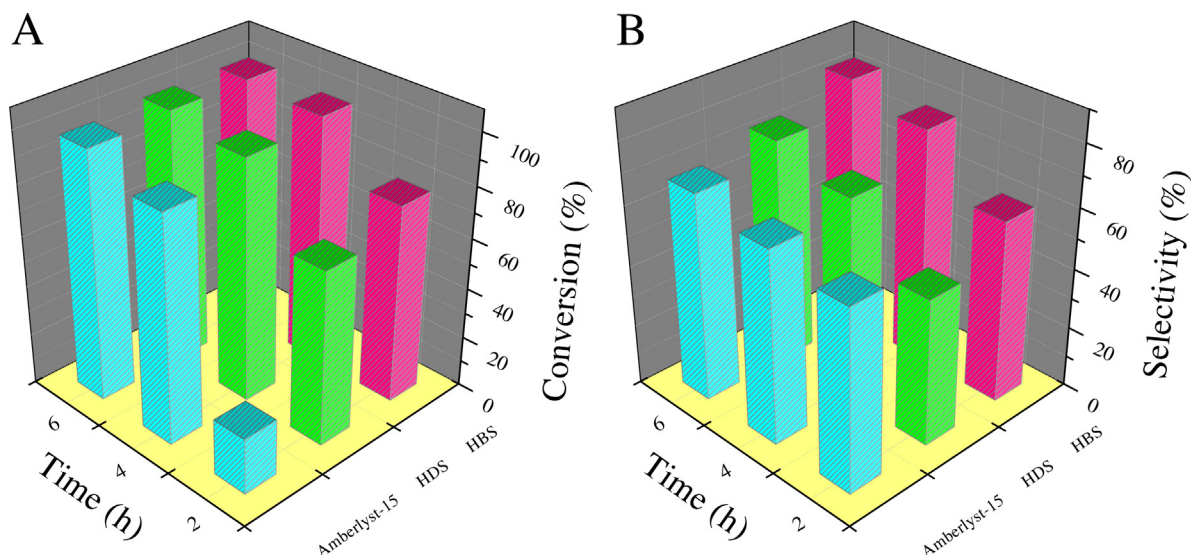


**Fig. 6.** (A) Conversion and (B) selectivity as the function of reaction time for Beckmann rearrangement of cyclohexanone oxime catalyzed by Amberlyst-15, HDS-4 and HBS-4.

ity of 61.3% over HDS-2 (run 3), and jumps to the high value 99.9% with selectivity of 89.0% and a high turnover number (TON) of 42.9 over HDS-4 (run 4). HDS-8 and HDS-16 keep the similarly high conversion but with declined selectivity (run 5 and 6). HBS-*x* series with more acid amount and stronger acid strength than HDS-*x*, exhibits superior activity. Even HBS-1 can present the high conversion of 99.9% with selectivity of 100% to target products MDM (run 8). Other HBS-*x* show consistent high conversion with complete selectivity (run 9–12). By comparison, classic solid acid catalysts such as H-beta (conversion 40.7% and selectivity 57.9%, run 13) and SBA-15-S (conversion 48.2% and selectivity 66.1%, run 14) exhibit inferior performances. Further, HBS-4 (run 10) is similar in activity to H<sub>2</sub>SO<sub>4</sub> (run 15) and Amberlyst-15 (run 16). Nevertheless, H<sub>2</sub>SO<sub>4</sub> is homogeneous and difficult to be isolated.

For HBS-4 and Amberlyst-15, on the other hand, the five-run recycling test (Fig. 5) indicates that HBS-4 can be reused steadily without apparent decline in activity while Amberlyst-15 shows drastic deactivation. After the five-run recycling test, the reused catalyst HBS-4 is characterized by FESEM image, FT-IR spectrum, N<sub>2</sub> sorption and elemental analysis. The FESEM image (Fig. S4A) shows the almost similar morphology of the reused HBS-4 sample to the fresh one, suggesting stable nanostructure for the reused catalyst. The FT-IR spectrum (Fig. S4B, curve b) depicts the same characteristic bands for the reused HBS-4 as the fresh one, reflecting the rare variation of the polymeric framework for the reused catalyst. N<sub>2</sub> sorption analysis (Fig. S5, curve d) indicates that the reused sample also presents type IV isotherm with similar hysteresis loop to the fresh one. The BET surface area and total pore volume of the reused sample are 805 m<sup>2</sup> g<sup>−1</sup> and 0.61 cm<sup>3</sup> g<sup>−1</sup>, respectively, indicating that the meso-structure is preserved on the reused sample, in according with the result of FESEM image. In the elemental analysis result for the reused HBS-4 that finds C 75.9%, H 3.8%, and S 6.9% (Table S1, entry 11), the molecular ratio of S to C is 0.0341, very close to the value over the fresh catalyst (0.0348), revealing the retaining of the sulfonic group on the reused HBS-4 samples. Briefly, the above analyses indicate the well preservation of the structure for the reused HBS-4 sample, verifying that our catalyst is effective and stable for this acid-catalyzed reaction with bulky substrate molecules.

All the above samples are also catalytically evaluated in another important acid-catalyzed reaction of liquid phase Beckmann rearrangement of cyclohexanone oxime, which produces the valuable raw material of  $\epsilon$ -caprolactam for synthesizing nylon-6. The reac-

**Table 3**

Catalytic activities of various HCP-based materials and control samples for Beckmann rearrangement of cyclohexanone oxime.<sup>a</sup>

Run	Catalyst	Con. (%) <sup>b</sup>	Sel. CPL (%) <sup>c</sup>	TON <sup>d</sup>
1	HD	0	–	0
2	HDS-1	98.1	65.5	9.89
3	HDS-2	99.9	69.3	8.77
4	HDS-4	99.9	74.9	8.90
5	HDS-8	99.9	66.9	8.16
6	HDS-16	99.9	63.0	7.50
7	HB	0	–	0
8	HBS-1	99.3	69.9	3.62
9	HBS-2	99.9	75.9	3.76
10	HBS-4	99.9	83.4	3.64
11	HBS-8	99.9	74.7	3.25
12	HBS-16	99.9	68.9	2.86
13	H-beta	50.6	63.7	2.66
14	SBA-15-S	79.2	57.2	3.54
15	H <sub>2</sub> SO <sub>4</sub>	99.9	69.0	0.34
16 <sup>e</sup>	H <sub>2</sub> SO <sub>4</sub>	33.0	46.9	0.68
17	Amberlyst-15	98.3	68.4	1.43
18 <sup>e</sup>	Amberlyst-15	52.1	59.7	1.36

<sup>a</sup> Reaction conditions: cyclohexanone oxime (1 mmol), benzonitrile (4 mL), catalyst (0.1 g), 130 °C, 6 h.

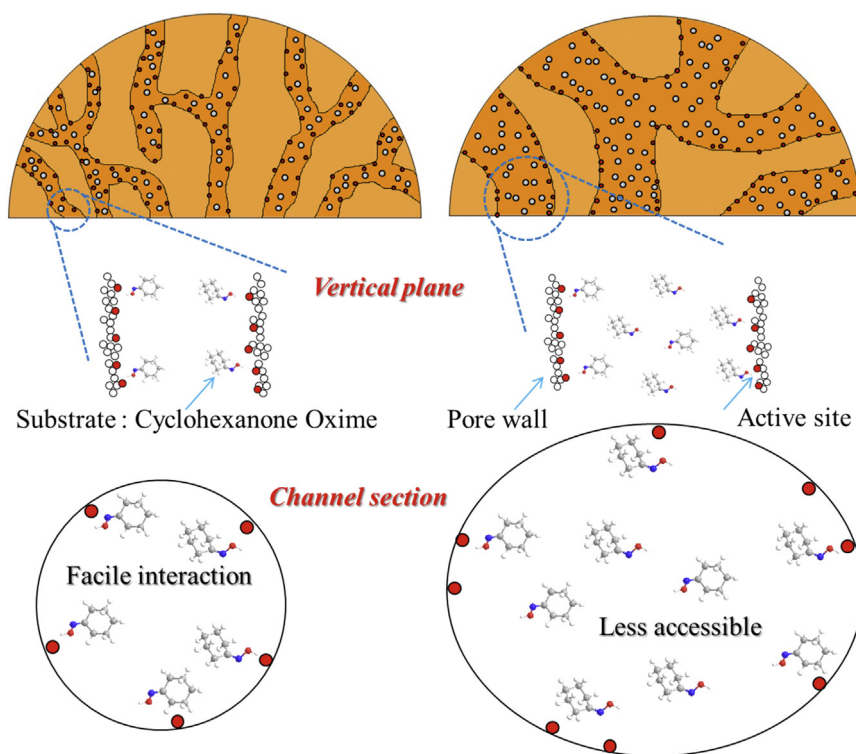
<sup>b</sup> Con. (%) = (mol  $\epsilon$ -caprolactam + mol cyclohexanone)/mol initial cyclohexanone oxime  $\times$  100.

<sup>c</sup> Sel. CPL (%) = mol  $\epsilon$ -caprolactam/(mol  $\epsilon$ -caprolactam + mol cyclohexanone)  $\times$  100.

<sup>d</sup> TON:  $\epsilon$ -caprolactam (mol) produced on per molar acid site.

<sup>e</sup> Reaction conditions: cyclohexanone oxime (1 mmol), benzonitrile (4 mL), catalyst (0.23 mmol H<sup>+</sup>), 130 °C, 6 h.

tion does not happen without a catalyst [54]. In Table 3, HD and HB which lack of acidic sites cannot catalyze the reaction (run 1 and 7). All the -SO<sub>3</sub>H-functionalized solid acid HDS-*x* samples present high conversions of more than 98.0% (run 2–6). The selectivity first arises and then declines slowly with increasing *x* numbers, and the maximum value of 74.9% is observed over HDS-4. Compared to HDS-*x*, HBS-*x* series demonstrate the same high conversion of more than 99.0% and superior selectivity (run 8–12). The highest selectivity of 83.4% is found over HBS-4, explicitly higher than H-beta (conversion 50.6% and selectivity 63.7%, run 13), SBA-15-S (conver-



**Scheme 2.** Schematic representation of the effect of the pore structure on the catalytic efficiency.

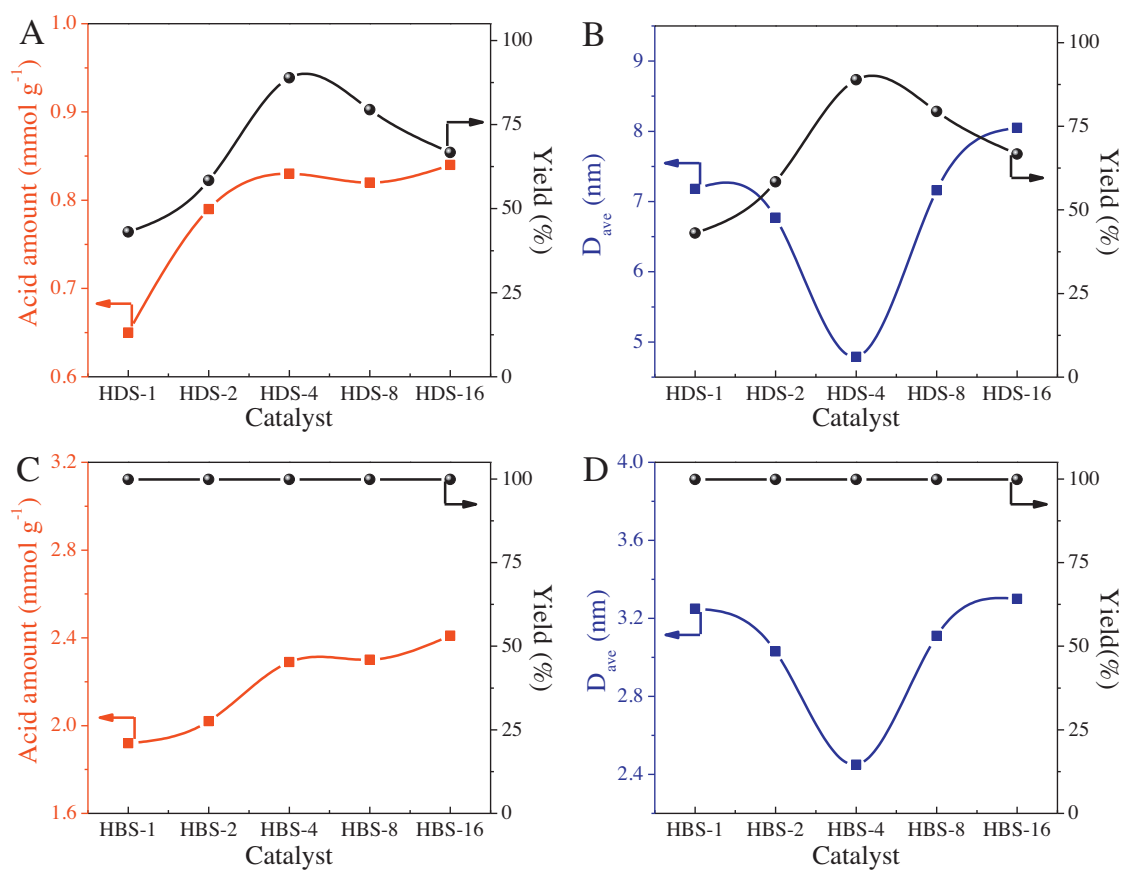


**Fig. 7.** Yield of Friedel–Crafts alkylation of anisole with benzyl alcohol as functions of acid amount and average pore diameter of (A and B) HDS-x and (C and D) HBS-x.

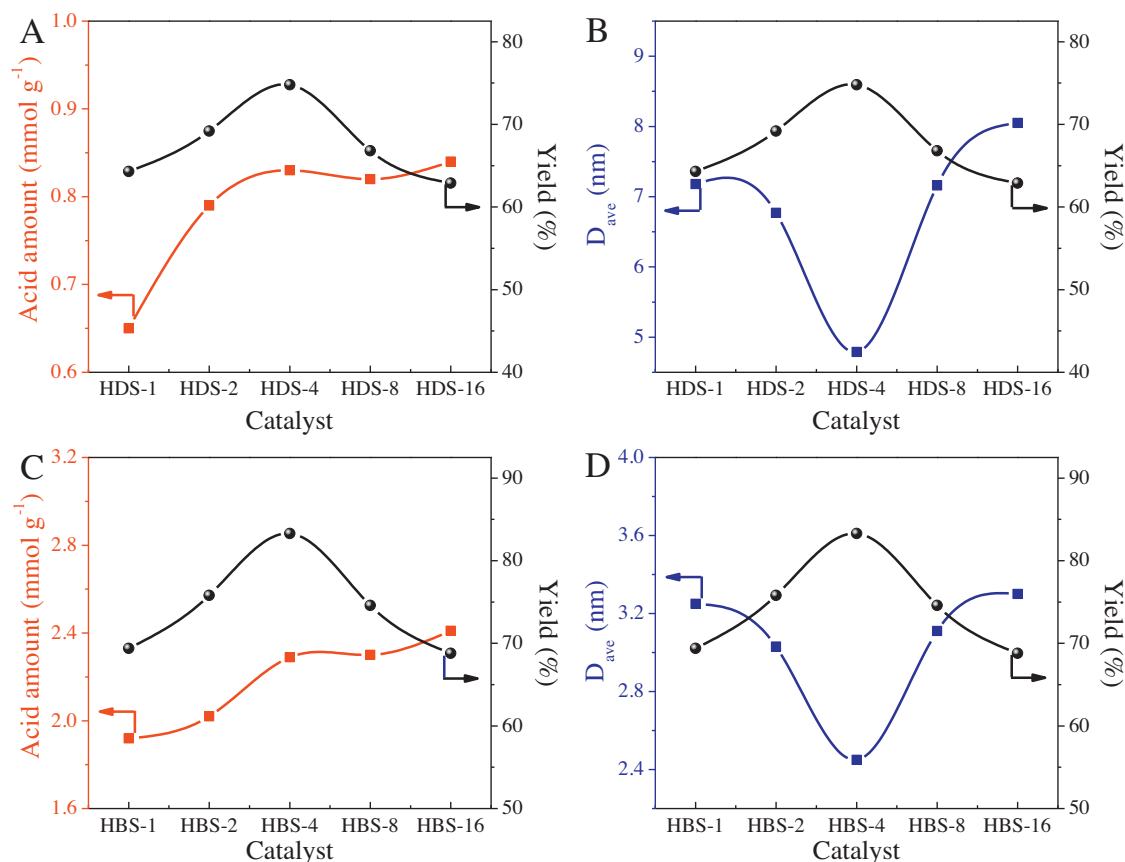


Fig. 8. Yield of Beckmann rearrangement of cyclohexanone oxime as functions of acid amount and average pore diameter of (A and B) HDS-*x* and (C and D) HBS-*x*.

sion 79.2% and selectivity 57.2%, run 14), Amberlyst-15 (conversion 98.3% and selectivity 68.4%, run 17), and even homogeneous H<sub>2</sub>SO<sub>4</sub> (conversion 99.9% and selectivity 69.0%, run 15). Notably, the above comparison is under the condition of using a same catalyst amount, where H<sub>2</sub>SO<sub>4</sub> and Amberlyst-15 contain much more acidic sites than HBS-*x* samples. If H<sub>2</sub>SO<sub>4</sub> and Amberlyst-15 included the same amount of acidic sites as HBS-4 assessed in the reaction, the former two catalysts show much more inferior activities (run 16 and 18): conversion 33.0% and selectivity 46.9% over H<sub>2</sub>SO<sub>4</sub>, and conversion 52.1% and selectivity 59.7% over Amberlyst-15. Furthermore, catalytic kinetics tests (Fig. 6) indicate that HDS-4 and HBS-4 exhibit much more rapid converting rate than Amberlyst-15 in early reaction period even using the same catalyst amount. For example, the conversion at 2 h is 22.1, 68.6 and 78.0% over Amberlyst-15, HDS-4 and HBS-4, respectively. Such results also demonstrate a more rapid rate over HBS-4 than HDS-4. All the comparisons allow drawing that the obtained HCP-based solid acids are efficient catalysts in the liquid-phase Beckmann rearrangement of cyclohexanone oxime, especially the HBS-4 sample.

### 3.5. Discussion

Liquid–solid heterogeneous catalysis usually involves mass transfer process crossing the interface of the two phases, thus the accessibility of substrates to active sites on the surface of pore channels of a solid catalyst significantly affects the catalytic performance [55,56]. In this work, the well catalytic performance of the -SO<sub>3</sub>H functionalized HCP-based solid acids can be attributed to high acidic density and narrow dispersed pores sized in the junc-

tion of micro and mesopores, in addition to large surface area of the polymeric framework.

Sulfonated mesoporous silica SBA-15-S has a large-surface-area inorganic framework but with lower acidic density, and conventional solid acid resin Amberlyst-15 has higher acid content (4.7 mmol g<sup>-1</sup>) but with much lower surface area (45 m<sup>2</sup> g<sup>-1</sup>). Therefore, they present inferior catalytic performance than HDS-*x* and HBS-*x* series which provide well accessibility of the organic substrates to active sites because of the high dispersion of abundant acidic sites on the organic polymeric matrix with very large surface areas. In addition to the above reason, the superior catalytic results of our HCP-based solid acid catalysts are also related to the nano-confinement effect depicted in Scheme 2. In the case of small pore size, only a limited amount of substrate molecules such as cyclohexanone oxime can be accommodated within the inner pore space, promoting the efficient collision of the substrate to the acidic site on the pore wall, which thereby accelerates the reaction [57–59]. By contrast, in the case of broad pores, the substrate not only attacks the acid site on the pore wall to proceed catalysis, but also can randomly cross the pore channel without react with acid sites, which causes a low catalytic efficiency. In this work, HDS-*x* and HBS-*x* series possess narrow size distribution with the most probable pore diameter at the junction value of micro and mesopores of ca. 2 nm. Such specific pore structure is recognized to provide a unique nano-confinement effect as illustrated in the former case of Scheme 2.

In order to clearly describe above nano-confinement effect, we plot dependence of yields as functions of acid amount and average pore diameter of HDS-*x*/HBS-*x* for Friedel–Crafts alkylation

(Fig. 7) and Beckmann rearrangement (Fig. 8), respectively. Since HDS- $x$  and HBS- $x$  possess similar polymeric frameworks and large surface areas, the variation of their catalytic performances should arise from their difference in acid amount and pore structure. In terms of acid sites, it is general that a larger amount of acid sites favor the better catalytic performance, which explains the following two results of this work: i) HBS- $x$  with larger amount of acid sites than HDS- $x$  exhibit higher activities; ii) the activity increases along with increasing the acid amount for Beckmann rearrangement over HDS- $x$ /HBS- $x$  ( $x \leq 4$ ) (Fig. 8A and C), which is also true for Friedel–Crafts alkylation over HDS- $x$  ( $x \leq 4$ ) (Fig. 7A). However a large amount of acid sites does not always lead to a higher catalytic activity, especially for the samples with  $x = 4, 8$  and  $16$  (Figs. 7A, 8A and C). The results imply that pore structures may play a significant role in affecting catalytic behaviors. HDS- $x$ /HBS- $x$ , along with increasing the amount of  $\text{ClSO}_3\text{H}$  used in the post-sulfonation treatment ( $x$ ), the pore size distribution first become narrower and when  $x \geq 4$  it turns out to be broader, reflected by the variation of average pore size diameter summarized in Table 1. The narrow distributed pore size can provide special nano-confinement effect to promote the reaction as illustrated in Scheme 2. Therefore, the decline of activities in the case of  $x > 4$  can be assigned to the broader of the pore size distribution that should weaken the nano-confinement effect. Taking the average pore size diameter ( $D_{\text{ave}}$ ) as the parameter to simply reflect the broad degree of overall pores, it is clearly that the smaller  $D_{\text{ave}}$  favors the higher yield (Figs. 7B, 8B and D). Therefore, the well catalytic performances of HDS-4 and HBS-4 within their individual series are ascribed to the narrow dispersed pores centered at the junction region of the micro and mesopores *ca.* 2 nm, and HBS-4 with the much enhanced acid amount exhibit higher activity than HDS-4. On the other hand, an exception is observed in HBS-catalyzed Friedel–Crafts alkylation, where all the HBS- $x$  members show similarly high activity whatever acid amount and pore size distribution change (Fig. 7C and D). It is known that Friedel–Crafts alkylation requires strong acidic catalysts and the reactivity may be dominated by the stronger and much more abundant acid sites [60,61] ( $>1.90 \text{ mmol/g}$ ) possessed by HBS- $x$  series, which is different from the catalysis of Beckmann rearrangement [54,62].

Aiming to support above speculation, a mesoporous PDVB sample is synthesized by polymerization of DVB and applied to prepare a polymeric solid acid through the same post-sulfonation route [44]. The obtained PDVB sample has the same polymeric framework composed of cross-linked benzene rings as HD and HB, therefore, the skeleton of the acidic PDVBS can be comparable with HDS and HBS.  $\text{N}_2$  sorption analysis for PDVBS (Fig. S5A, curve a) shows type IV isotherm. Moreover, PDVBS has large BET surface area ( $543 \text{ m}^2 \text{ g}^{-1}$ ) and total pore volume ( $1.31 \text{ cm}^3 \text{ g}^{-1}$ ), but possesses wide pore dispersion with the average pore diameter of 9.66 nm (Fig. S5 and Table S3), which is expected to hardly provide the special nano-confined effect. Indeed, inferior activity (yield 62.0%, Table S3) is observed over PDVBS with the acid amount of  $2.29 \text{ mmol g}^{-1}$  in the Beckmann rearrangement reaction, much lower than that over HBS-4 (yield 83.4%) with narrow dispersed pores and same acid amount at the same reaction condition. Additional comparison is made between PDVBS and HDS-16. PDVBS has similar average pore diameter (9.66 nm) as HDS-16 (8.05 nm), but the latter contains a large proportion of smaller pores sized at *ca.* 1.89 nm, differing from the situation over the former. When assessed in Beckmann rearrangement at the earlier reaction period of 4 h, HDS-16 offers much higher yield (56.4%) and TON (6.71) than PDVBS (yield 46.7% and TON 2.04) (Table S3). The above phenomena further indicate that the present HCP-based solid acid catalysts are able to provide special nano-confinement effect that is beneficial in promoting catalytic activities.

#### 4. Conclusion

In summary, we have developed an unprecedented strategy for constructing  $-\text{SO}_3\text{H}$ -bearing highly crosslinked porous organic polymers and demonstrated their utility as heterogeneous carbocatalysts for acid-catalyzed reactions. These novel solid acids are fabricated on the basis of self-condensation of bischloromethyl monomers and functionality with chlorosulfonic acid. The pore structure and acidic amount can be adjusted by monomer selection and sulfonation degree. High concentrations of active  $-\text{SO}_3\text{H}$  sites are covalently attached to the polymer skeletons with high surface areas. In addition, narrow dispersed pores located in the junction region of micro and mesopores (*ca.* 2 nm) can be achieved on these HCP-based solid acids, providing special nano-confinement effect in catalysis. Therefore, these solid acids present excellent catalytic activities and good recyclability in Friedel–Crafts reaction and Beckmann rearrangement. The optimal sample HBS-4 shows a high conversion of 99.9% with selectivity of 100% at 4 h and  $120^\circ\text{C}$  when catalyzing the reaction of anisole with benzyl alcohol, and offers an amazing conversion of 99.9% with selectivity of 83.4% for rearranging cyclohexanone oxime. This work develops an efficient way to fabricate functionalized materials from porous hypercrosslinked polymers for metal-free catalytic reactions.

#### Acknowledgements

The authors thank greatly the National Natural Science Foundation of China (Nos. 21136005, 21303084 and 21476109), Jiangsu Provincial Science Foundation for Youths (No. BK20130921), Specialized Research Fund for the Doctoral Program of Higher Education (No. 20133221120002), and the funding of the Scientific Research and Innovation Project for College Graduates of Jiangsu Province (CXZZ13.0445).

#### Appendix A. Supplementary data

Supplementary data associated with this article can be found, in the online version, at <http://dx.doi.org/10.1016/j.apcatb.2015.04.054>.

#### References

- [1] D.R. Dreyer, H. Jia, C.W. Bielawski, *Angew. Chem. Int. Ed.* 49 (2010) 6813–6816.
- [2] M. Soria-Sánchez, A. Maroto-Valiente, J. Álvarez-Rodríguez, V. Munoz-Andrés, I. Rodríguez-Ramos, A. Guerrero-Ruiz, *Appl. Catal. B: Environ.* 104 (2011) 101–109.
- [3] A. Modak, J. Mondal, A. Bhaumik, *ChemCatChem* 5 (2013) 1749–1753.
- [4] S. Navalón, A. Dhakshinamoorthy, M. Alvaro, H. García, *Chem. Rev.* 114 (2014) 6179–6212.
- [5] D. Su, J. Zhang, B. Frank, A. Thomas, X. Wang, J. Paraknowitsch, R. Schlögl, *ChemSusChem* 3 (2010) 169–180.
- [6] J. Zhu, P. Xiao, H. Li, S.A.C. Carabineiro, *ACS Appl. Mater. Interfaces* 6 (2014) 16449–16465.
- [7] M. Kitano, K. Arai, A. Kodama, T. Kousaka, K. Nakajima, S. Hayashi, M. Hara, *Catal. Lett.* 131 (2009) 242–249.
- [8] K. Fukuhara, K. Nakajima, M. Kitano, H. Kato, S. Hayashi, M. Hara, *ChemSusChem* 4 (2011) 778–784.
- [9] A. Thomas, *Angew. Chem. Int. Ed.* 49 (2010) 8328–8344.
- [10] D. Yu, E. Nagelli, F. Du, L. Dai, *J. Phys. Chem. Lett.* 1 (2010) 2165–2173.
- [11] A. Rey, J.A. Zazo, J.A. Casas, A. Bahamonde, J.J. Rodríguez, *Appl. Catal. A: Gen.* 402 (2011) 146–155.
- [12] X. Li, X. Wang, M. Antonietti, *ACS Catal.* 2 (2012) 2082–2086.
- [13] R.K. Totten, Y.S. Kim, M.H. Weston, O.K. Farha, J.T. Hupp, S.T. Nguyen, *J. Am. Chem. Soc.* 135 (2013) 11720–11723.
- [14] Y. Wang, H. Li, J. Yao, X. Wang, M. Antonietti, *Chem. Sci.* 2 (2011) 446–450.
- [15] H. Zhao, H. Yu, X. Quan, S. Chen, Y. Zhang, H. Zhao, H. Wang, *Appl. Catal. B: Environ.* 152–153 (2014) 46–50.
- [16] P. Kaur, J.T. Hupp, S.T. Nguyen, *ACS Catal.* 1 (2011) 819–835.
- [17] Y. Zhang, S.N. Riduan, *Chem. Soc. Rev.* 41 (2012) 2083–2094.
- [18] Q. Chen, D. Liu, J. Zhu, B. Han, *Macromolecules* 47 (2014) 5926–5931.
- [19] A. Modak, M. Pramanik, S. Inagaki, A. Bhaumik, *J. Mater. Chem. A* 2 (2014) 11642–11650.



- [20] H.C. Cho, H.S. Lee, J. Chun, S.M. Lee, H.J. Kim, S.U. Son, *Chem. Commun.* 47 (2011) 917–919.
- [21] E. Andrijanto, E.A. Dawson, D.R. Brown, *Appl. Catal. B: Environ.* 115 (2012) 261–268.
- [22] Y. Zhang, S.A.Y. Zou, X. Luo, Z. Li, H. Xia, X. Liu, Y. Mu, *J. Mater. Chem. A* 2 (2014) 13422–13430.
- [23] A. Thomas, A. Fischer, F. Goettmann, M. Antonietti, J.O. Müller, R. Schlögl, J.M. Carlsson, *J. Mater. Chem.* 18 (2008) 4893–4908.
- [24] J. Schmidt, D.S. Kundu, S. Blechert, A. Thomas, *Chem. Commun.* 50 (2014) 3347–3349.
- [25] Y. Zhang, Y. Zhang, Y.L. Sun, X. Du, J.Y. Shi, W.D. Wang, W. Wang, *Chem. Eur. J.* 18 (2012) 6328–6334.
- [26] E. Merino, E. Verde-Sesto, E.M. Maya, M. Iglesias, F. Sánchez, A. Corma, *Chem. Mater.* 25 (2013) 981–988.
- [27] S. Xu, Y. Luo, B. Tan, *Macromol. Rapid Commun.* 34 (2013) 471–484.
- [28] E.M. Sulman, V.G. Matveeva, V.Y. Doluda, A.I. Sidorov, N.V. Lakina, A.V. Bykov, M.G. Sulman, P.M. Valetsky, L.M. Kustov, O.P. Tkachenko, B.D. Stein, L.M. Bronstein, *Appl. Catal. B: Environ.* 94 (2010) 200–210.
- [29] R. Dawson, T. Ratvijitvech, M. Corker, A. Laybourn, Y.Z. Khimyak, A.I. Cooper, D.J. Adams, *Polym. Chem.* 3 (2012) 2034–2038.
- [30] E.M. Sulman, V.G. Matveeva, V.Y. Doluda, A.I. Sidorov, N.V. Lakina, A.V. Bykov, M.G. Sulman, P.M. Valetsky, L.M. Kustov, O.P. Tkachenko, B.D. Stein, L.M. Bronstein, *Appl. Catal. B: Environ.* 94 (2010) 200–210.
- [31] B. Li, Z. Guan, W. Wang, X. Yang, J. Hu, B. Tan, T. Li, *Adv. Mater.* 24 (2012) 3390–3395.
- [32] C.D. Wood, B. Tan, A. Trewin, H. Niu, D. Bradshaw, M.J. Rosseinsky, Y.Z. Khimyak, N.L. Campbell, R. Kirk, E. Stöckel, A.I. Cooper, *Chem. Mater.* 19 (2007) 2034–2048.
- [33] G. Liu, Y. Wang, C. Shen, Z. Ju, D. Yuan, *J. Mater. Chem. A* 3 (2015) 3051–3058.
- [34] Y. Yang, Q. Zhang, S. Zhang, S. Li, *RSC Adv.* 4 (2014) 5568–5574.
- [35] Y. Yang, Q. Zhang, S. Zhang, S. Li, *Polymer* 54 (2013) 5698–5702.
- [36] Y. Zhang, S. Wei, F. Liu, Y. Du, S. Liu, Y. Ji, T. Yokoi, T. Tatsumi, F. Xiao, *Nano Today* 4 (2009) 135–142.
- [37] D. Margolese, J.A. Melero, S.C. Christiansen, B.F. Chmelka, G.D. Stucky, *Chem. Mater.* 12 (2000) 2448–2459.
- [38] S. Saravanamurugan, M. Palanichamy, M. Hartmann, V. Murugesan, *Appl. Catal. A: Gen.* 298 (2006) 8–15.
- [39] J. Chen, K. Li, L. Chen, R. Liu, X. Huang, D. Ye, *Green Chem.* 16 (2014) 2490–2499.
- [40] J. Li, Y. Zhou, D. Mao, G. Chen, X. Wang, X. Yang, M. Wang, L. Peng, J. Wang, *Chem. Eng. J.* 254 (2014) 54–62.
- [41] R. Xing, N. Liu, Y. Liu, H. Wu, Y. Jiang, L. Chen, M. He, P. Wu, *Adv. Funct. Mater.* 17 (2007) 2455–2461.
- [42] T.M. Suzuki, T. Nakamura, E. Sudo, Y. Akimoto, K. Yano, *J. Catal.* 258 (2008) 265–272.
- [43] F. Liu, W. Kong, L. Wang, X. Yi, I. Noshadi, A. Zheng, C. Qi, *Green Chem.* 17 (2015) 480–489.
- [44] F. Liu, X. Meng, Y. Zhang, L. Ren, F. Nawaz, F. Xiao, *J. Catal.* 271 (2010) 52–58.
- [45] F. Liu, A. Zheng, I. Noshadi, F. Xiao, *Appl. Catal. B: Environ.* 136 (2013) 193–201.
- [46] J. Pan, H. Gao, Y. Zhang, J. Zeng, W. Shi, C. Song, Y. Yan, L. Yu, D. Chang, *RSC Adv.* 4 (2014) 59175–59184.
- [47] Z. Wei, Y. Yang, Y. Hou, Y. Liu, X. He, S. Deng, *ChemCatChem* 6 (2014) 2354–2363.
- [48] L. Li, H. Ren, Y. Yuan, G. Yu, G. Zhu, *J. Mater. Chem. A* 2 (2014) 11091–11098.
- [49] S. Ren, R. Dawson, A. Laybourn, J. Jiang, Y. Khimyak, D.J. Adams, A.I. Cooper, *Polym. Chem.* 3 (2012) 928–934.
- [50] Y. Xu, L. Chen, Z. Guo, A. Nagai, D. Jiang, *J. Am. Chem. Soc.* 133 (2011) 17622–17625.
- [51] K.H. Chung, D.R. Chang, B.G. Park, *Bioresour. Technol.* 99 (2008) 7438–7443.
- [52] G.V.A. Martins, G. Berlier, C. Bisio, S. Coluccia, H.O. Pastore, L. Marchese, *J. Phys. Chem. C* 112 (2008) 7193–7200.
- [53] Y. Zhang, W. Wong, K. Yung, *Appl. Energy* 116 (2014) 191–198.
- [54] D. Mao, Z. Long, Y. Zhou, J. Li, X. Wang, J. Wang, *RSC Adv.* 4 (2014) 15635–15641.
- [55] L. Chen, Y. Yang, D. Jiang, *J. Am. Chem. Soc.* 132 (2010) 9138–9143.
- [56] A. Schtz, O. Reiser, W.J. Stark, *Chem. Eur. J.* 16 (2010) 8950–8967.
- [57] R. Xiang, Z. Yang, Q. Zhang, G. Luo, W. Qian, F. Wei, M. Kadowaki, E. Einarsson, S. Maruyama, *J. Phys. Chem. C* 112 (2008) 4892–4896.
- [58] Y. Choi, H. Park, Y.S. Yun, J. Yi, *ChemSusChem* 8 (2015) 974–979.
- [59] P. Zhang, T. Wu, M. Hou, J. Ma, H. Liu, T. Jiang, W. Wang, C. Wu, B. Han, *ChemCatChem* 6 (2014) 3323–3327.
- [60] K. Leng, Y. Wang, C. Hou, C. Lancelot, C. Lamonier, A. Rives, Y. Sun, *J. Catal.* 306 (2013) 100–108.
- [61] Ch. R. Kumar, P.S.S. Prasad, N. Lingaiah, *Appl. Catal. A: Gen.* 384 (2010) 101–106.
- [62] N.R. Shiju, H.M. Williams, D.R. Brown, *Appl. Catal. B: Environ.* 90 (2009) 451–457.